

星形成ゼミ

2017/11/10

SFN #297 #6-#10

長谷川哲夫(国立天文台)

297  
#6

# Methanol masers reveal the magnetic field of the high-mass protostar IRAS 18089-1732

D. Dall'Olio, W. H. T. Vlemmings, G. Surcis, H. Beuther, B. Lankhaar<sup>1</sup>, M. V. Persson, A. M. S. Richards, and E. Varenus  
arXiv:1708.02961v1

## ABSTRACT

*Context.* The importance of the magnetic field in high-mass-star formation is not yet fully clear and there are still many open questions concerning its role in the accretion processes and generation of jets and outflows. In the past few years, masers have been successfully used to probe the magnetic field morphology and strength at scales of a few au around massive protostars, by measuring linear polarisation angles and Zeeman splitting. The massive protostar IRAS 18089-1732 is a well studied high-mass-star forming region, showing a hot core chemistry and a disc-outflow system. Previous SMA observations of polarised dust revealed an ordered magnetic field oriented around the disc of IRAS 18089-1732.

*Aims.* We want to determine the magnetic field in the dense region probed by 6.7 GHz methanol maser observations and compare it with observations in dust continuum polarisation, to investigate how the magnetic field in the compact maser region relates to the large-scale field around massive protostars.

*Methods.* We reduced MERLIN observations at 6.7 GHz of IRAS 18089-1732 and we analysed the polarised emission by methanol masers.

*Results.* Our MERLIN observations show that the magnetic field in the 6.7 GHz methanol maser region is consistent with the magnetic field constrained by the SMA dust polarisation observations. A tentative detection of circularly polarised line emission is also presented.

*Conclusions.* We found that the magnetic field in the maser region has the same orientation as in the disk. Thus the large-scale field component, even at the au scale of the masers, dominates over any small-scale field fluctuations. We obtained, from the circular polarisation tentative detection, a field strength along the line of sight of 5.5 mG which appeared to be consistent with the previous estimates.

**Key words.** magnetic field – stars: formation – stars: massive – masers – polarization

大質量星形成領域 IRAS 18089-1732 ( $L = 12.89d$ ,  $B = +0.50d$ )

- 距離 2.34 kpc,  $L = 1.3E4 L_{\text{sun}}$ ,  $M_{\text{gas}} \sim 1E3 M_{\text{sun}}$
- Disk + outflow (南北方向)

SMAでの観測 (Beuther+ 2010)

- Diskのdust continuum偏波 → diskに沿った磁場 (Chandrasekhar-Fermi法で  $B_{\text{pos}} \sim 11$  mG)
- OutflowのCO 3-2でGoldreich-Kylafis効果 ( $P \sim 8\%$ )

CH<sub>3</sub>OH 6.7 GHz maserのモニター (Goedhart+ 2009) → 29.5日周期の強度変動

観測

6.7 GHz CH<sub>3</sub>OH maser  
MERLIN  
2008年3月, 4月, 7月  
Beam 0.18" x 0.03"

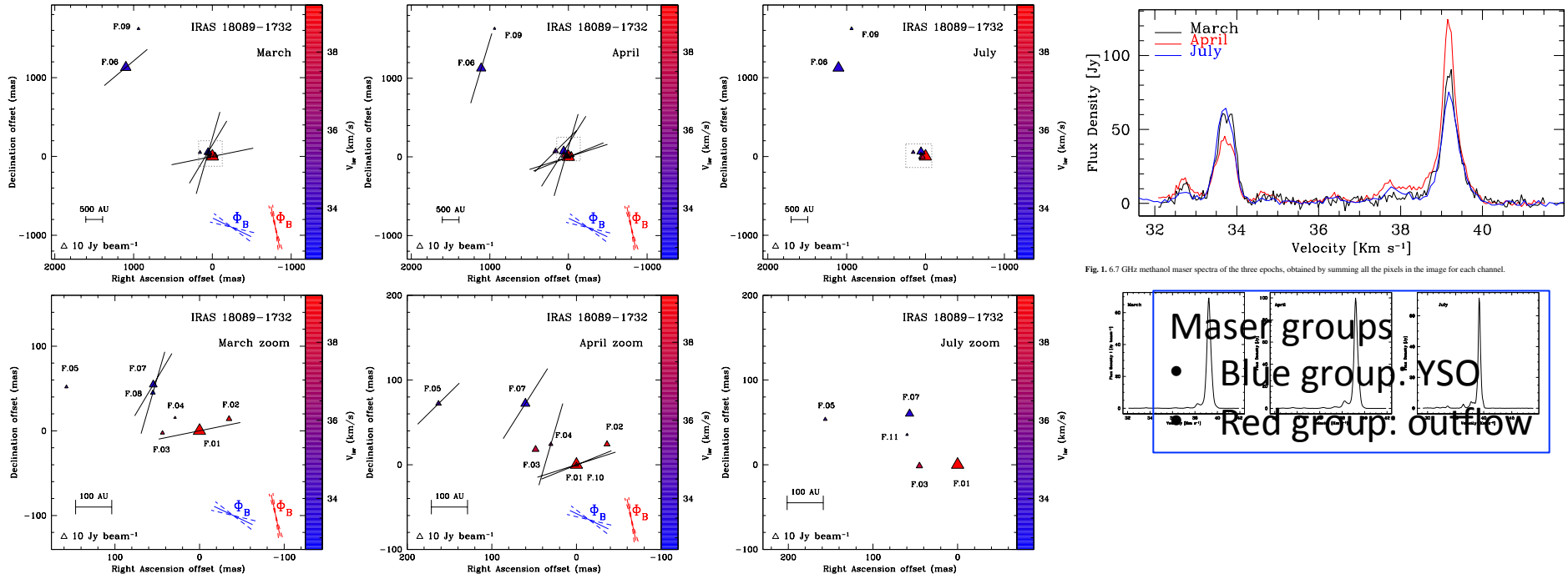


**Fig. 3.** Masers identified in March (left), April (centre) and July (right) as listed in Table 3–5. The bottom panel shows a zoom of the region marked by the dashed grey boxes in the top panels. Each maser is represented by a triangle. The different sizes of the triangles represent the intensity, while the colours indicate the velocity of the maser feature, according to the scale reported in the colour bar. Line segments mark the direction of the polarisation angle for the maser features that show linear polarisation. The average direction of the resulting magnetic field  $\Phi_B$  obtained for two groups of masers as defined in Sect. 5.2 is indicated in the bottom right corners of each panel. The July observations were in dual circular polarisation only.

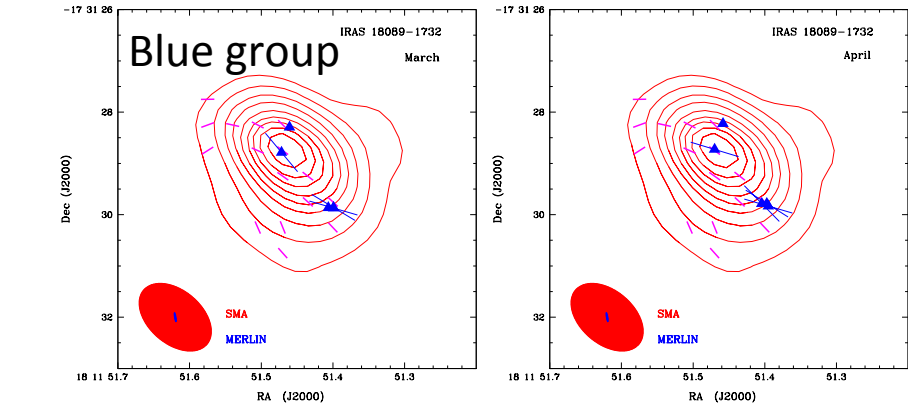


**Fig. 4.** Masers in the blue group (blue triangles and blue segments) superimposed on the integrated I image of the dust continuum emission observed by Beuther et al. (2010) at  $880 \mu\text{m}$  with SMA (red contours; the contours are drawn in  $10\sigma$  steps). The magenta line segments show the magnetic field orientation obtained by linearly polarised dust emission (Beuther et al. 2010). The blue segments represent the magnetic field orientation obtained by our linearly polarised methanol maser emission (Sect. 5.2); therefore the magnetic field follows the same direction indicated by the dust emission. The red and blue ellipses show the beams of SMA ( $1.65'' \times 1.05''$ , position angle  $51^\circ$ ) and MERLIN, respectively. Left panel: March; right panel: April.

## Zeeman - Tentative detection (再現せず)

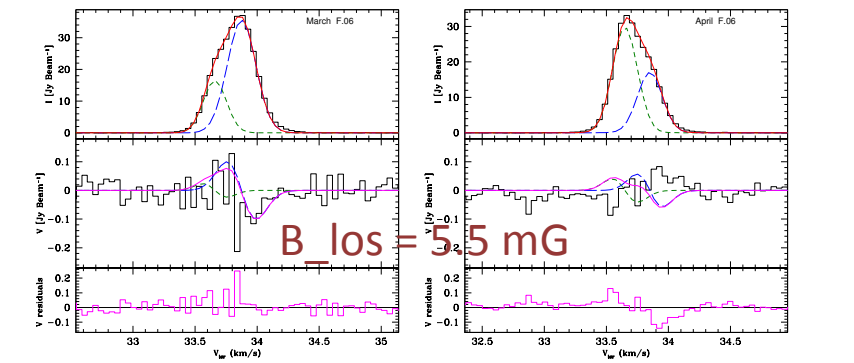


**Fig. 6.** Fit to maser feature F.06 assuming the presence of two hyperfine components; left: March observation, right: April observation. Upper panels: total intensity I spectrum plotted as the black histogram. The solid red curve in the upper panel is the best fit using two Gaussian components, representing two maser hyperfine components separated by  $0.2 \text{ km s}^{-1}$  (see Sect. 5.4). Component 1 is the blue long-dashed line and component 2 is the green short-dashed line. Middle panels: circular polarisation V spectrum (black histogram). The solid magenta line is the sum of the derivatives of the two components of the fit from the upper panel. The blue long-dashed line is the derivative of component 1 and the green short-dashed line is the derivative of component 2. Lower panels: we plot the residuals between the circular polarisation (middle panel, black histogram) and the sum of the derivatives (middle panel, solid magenta line).

297  
#7

## Photometric Determination of the Mass Accretion Rates of Pre-main-sequence Stars. V. Recent Star Formation in the 30 Dor Nebula

Guido De Marchi, Nino Panagia, and Giacomo Beccari  
ApJ 846, 110 (2017)

### Abstract

We report on the properties of the low-mass stars that recently formed in the central  $\sim 2'.7 \times 2'.7$  of 30 Dor, including the R136 cluster. Using the photometric catalog of De Marchi et al., based on observations with the *Hubble Space Telescope*, and the most recent extinction law for this field, we identify 1035 bona fide pre-main-sequence (PMS) stars showing  $H\alpha$  excess emission at the  $4\sigma$  level with an  $H\alpha$  equivalent width of 20 Å or more. We find a wide spread in age spanning the range  $\sim 0.1$ –50 Myr. We also find that the older PMS objects are placed in front of the R136 cluster and are separated from it by a conspicuous amount of absorbing material, indicating that star formation has proceeded from the periphery into the interior of the region. We derive physical parameters for all PMS stars, including masses  $m$ , ages  $t$ , and mass accretion rates  $\dot{M}_{\text{acc}}$ . To identify reliable correlations between these parameters, which are intertwined, we use a multivariate linear regression fit of the type  $\log \dot{M}_{\text{acc}} = a \times \log t + b \times \log m + c$ . The values of  $a$  and  $b$  for 30 Dor are compatible with those found in NGC 346 and NGC 602. We extend the fit to a uniform sample of 1307 PMS stars with  $0.5 < m/M_{\odot} < 1.5$  and  $t < 16$  Myr in six star-forming regions in the Large and Small Magellanic Clouds and Milky Way with metallicities in the range of  $0.1$ – $1.0 Z_{\odot}$ . We find  $a = -0.59 \pm 0.02$  and  $b = 0.78 \pm 0.08$ . The residuals are systematically different between the six regions and reveal a strong correlation with metallicity  $Z$ , of the type  $c = (-3.69 \pm 0.02) - (0.30 \pm 0.04) \times \log Z/Z_{\odot}$ . A possible interpretation of this trend is that when the metallicity is higher so is the radiation pressure, and this limits the accretion process, in both its rate and duration.

*Key words:* galaxies: star clusters: general – galaxies: star clusters: individual (30 Dor) – galaxies: stellar content – Magellanic Clouds – stars: formation – stars: pre-main sequence

HST multiband photometric catalog (De Marchi+ 2011)

- Concentrate on F555W (V), F814W (I), and F656N (H-alpha) bands

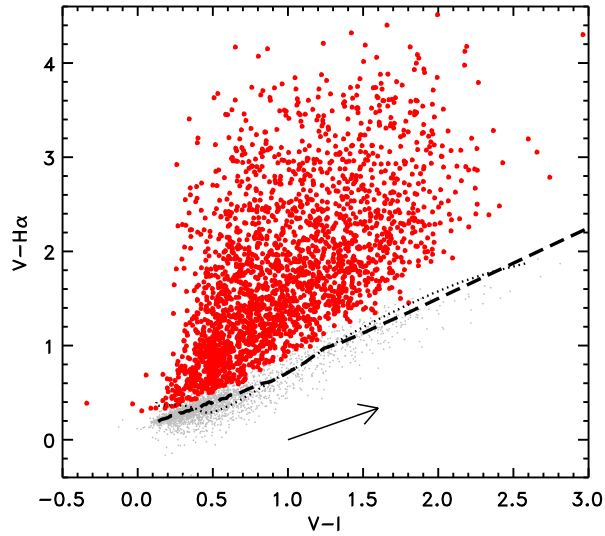


**Figure 2.** Identification of objects with excess H $\alpha$  emission. The dashed line is the median photospheric  $V - H\alpha$  color for stars with small ( $<0.05$  mag) combined photometric uncertainties in all three bands. For comparison, the dotted line shows the colors in these filters for the model atmospheres of Bessell et al. (1998). Thick filled circles denote stars with H $\alpha$  excess emission higher than the  $3\sigma$  level. The  $A_V = 1.8$  reddening vector is shown, as an example, for the 30 Dor extinction law.

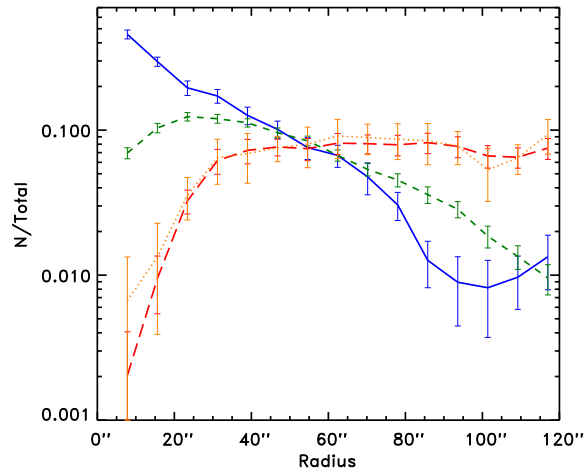


**Figure 4.** Radial distribution of UMS stars (solid blue line) and of low-mass PMS candidates younger than 5 Myr (short-dashed green line) and older than 5 Myr (long-dashed red line). The dotted line corresponds to stars with ages intermediate between 5 and 10 Myr. The curves are normalized by the number of objects in each sample, and the solid line is further rescaled by a factor of 0.65 for ease of comparison. Note that crowding is the cause of the apparent drop observed at small radii in the profiles of PMS stars (the effect is negligible for the much brighter and sparser UMS objects). Error bars correspond to the Poisson uncertainty on the number counts.

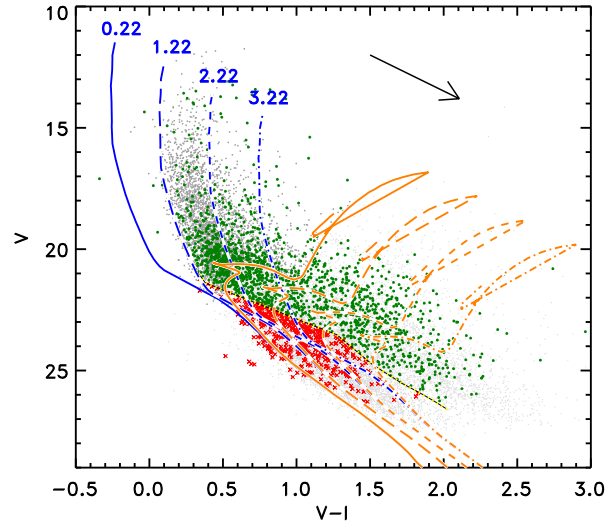


**Figure 3.** Same as Figure 1, but including all candidate PMS stars with H $\alpha$  excess emission and the isochrone for PMS age of 5 Myr (thin dashed line) for  $A_V = 1.22$ . Stars with H $\alpha$  excess emission located above and below the 5 Myr isochrone are indicated with green thick filled circles and red crosses, respectively, and are approximately younger and older than 5 Myr.

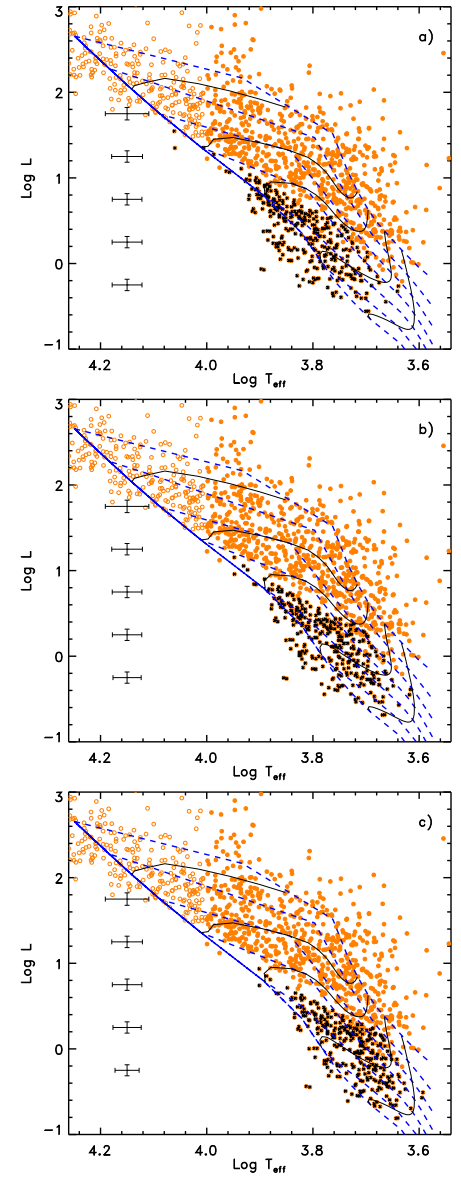


**Figure 5.** H-R diagram of the bona fide PMS stars (filled circles, with an additional cross if older than 5 Myr). Objects hotter than 10,000 K (open circles) are shown but not considered in this work. The typical  $\pm 1\sigma$  uncertainties on  $T_{\text{eff}}$  and  $L$  are shown by the error bars. The three panels correspond to different reddening values for the stars classified as older than 5 Myr in the CMD of Figure 3 (crosses). The adopted values are, respectively,  $A_V = 1.22$  (panel (a)), 0.72 (panel (b)), and 0.22 (panel (c)). The dashed lines are the PMS isochrones from the models of Tognelli et al. (2011), for ages of 1, 2, 4, 8, 16, 32, and 64 Myr, from right to left (note that where multiple isochrones reach the MS and overlap, lines appear solid instead of dashed). Also shown are the representative evolutionary tracks for masses of 0.7, 1, 1.5, 2, 3, and  $4 M_{\odot}$  (solid lines).

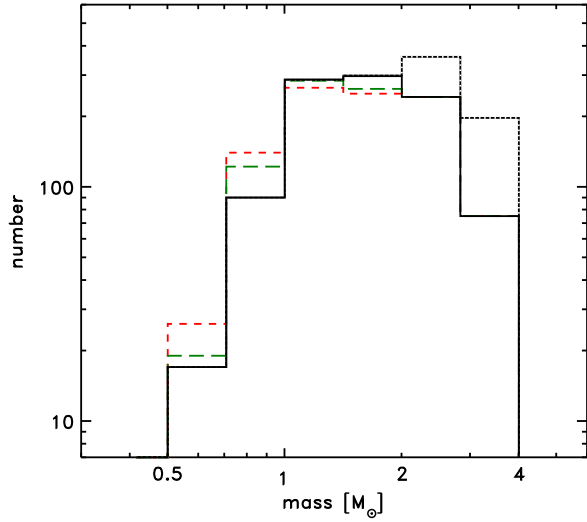


**Figure 6.** Histograms of the mass distribution for the 1035 bona fide PMS stars. Different line types correspond to different  $A_V$  choices for the older PMS objects:  $A_V = 1.22$  (solid line),  $A_V = 0.72$  (long-dashed line), and  $A_V = 0.22$  (short-dashed line). For completeness, the dotted line shows the mass distribution of the stars with  $H\alpha$  excess emission hotter than 10,000 K that we do not consider in this work.

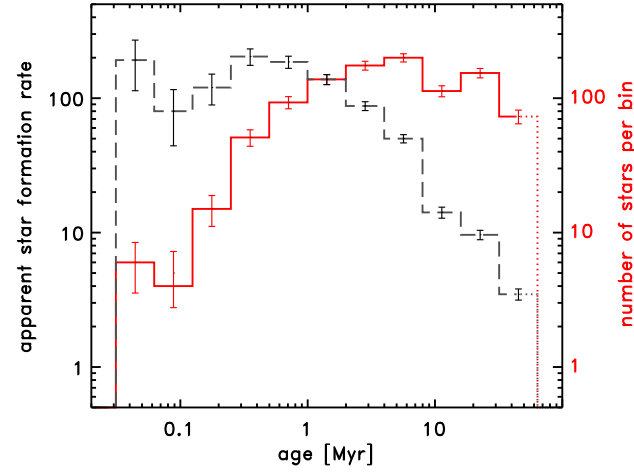


**Figure 7.** Histograms of the age distribution of PMS stars. A constant logarithmic step is used (factor of 2). The solid line provides the number of stars inside each age bin, while the dashed line shows the apparent star formation rate in units of  $\text{Myr}^{-1}$ .

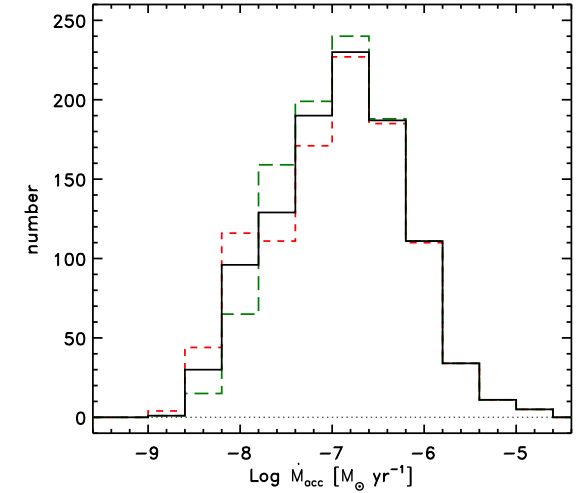


**Figure 8.** Histograms of the mass accretion rate values of the bona fide PMS stars. As before, different line types correspond to different  $A_V$  choices for the older PMS objects:  $A_V = 1.22$  (solid line),  $A_V = 0.72$  (long-dashed line), and  $A_V = 0.22$  (short-dashed line).

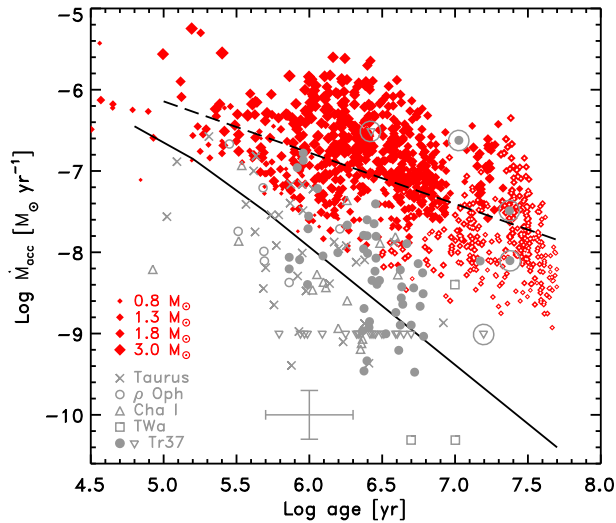


**Figure 9.** Mass accretion rates of bona fide PMS stars, as a function of stellar age. Diamonds refer to the objects in 30 Dor, and their size is proportional to the stellar mass (see legend). In this graph, we have adopted  $A_V = 0.72$  for all PMS stars older than 5 Myr (open diamonds). The dashed line represents the best fit to the 30 Dor data. Other symbols correspond to a sample of Galactic T Tauri stars from the literature, as per the legend (the large circles around some of the symbols indicate dwarfs of spectral type G in the Tr 37 sample). The solid line shows the relationship between  $\dot{M}_{\text{acc}}$  and  $t$  predicted by models of the evolution of a viscous disk (Hartmann et al. 1998).

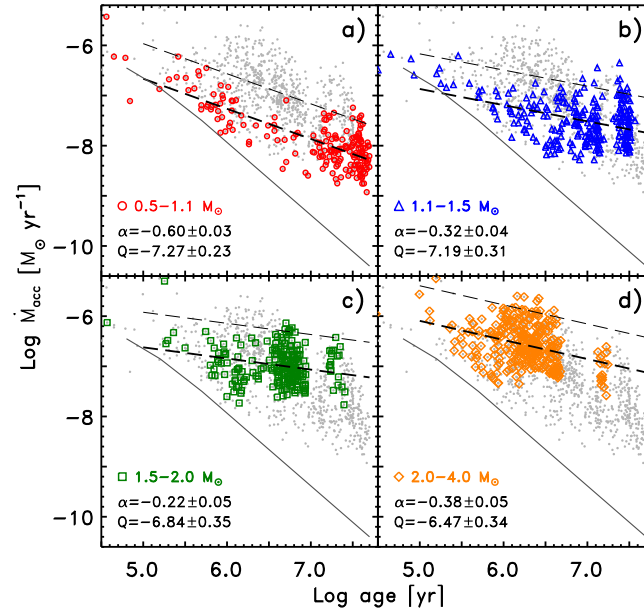


**Figure 10.** Same as Figure 9, but for stars in different mass groups, as indicated in each panel. The slope  $\alpha$  and intercept  $Q$  (at 1 Myr) of the best fits (thick dashed lines) are given in each panel. The values of  $\alpha$  are considerably shallower than the slope predicted by the models of Hartmann et al. (1998; solid line). The thin dashed lines represent the lines of best fit shifted vertically by 0.7 dex and define good envelopes to the observed distributions.

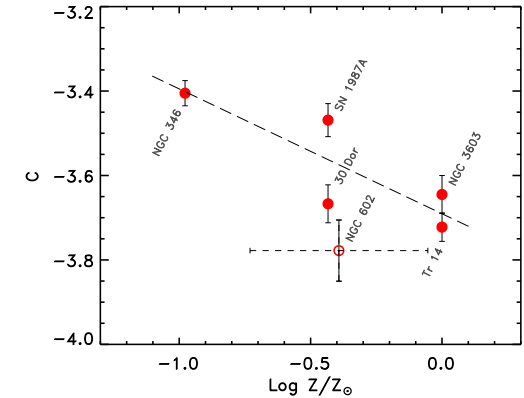


**Figure 11.** Effective mass accretion rate  $c$  shown as a function of the metallicity of the regions in our sample (see Table 1). Error bars correspond to  $\pm 2\sigma$ .

Yasui+ 2009,10,16の  
主張とは逆センス

297  
#8

## Embedded Filaments in IRAS 05463+2652: Early Stage of Fragmentation and Star Formation Activities

L. K. Dewangan , R. Devaraj , T. Baug , and D. K. Ojha  
ApJ 848, 51 (2017)

### Abstract

We present a multiwavelength data analysis of IRAS 05463+2652 (hereafter I05463+2652) to study star formation mechanisms. A shell-like structure around I05463+2652 is evident in the *Herschel* column density map, which is not associated with any ionized emission. Based on the *Herschel* submillimeter images, several parsec-scale filaments (including two elongated filaments, “s-fl” and “nw-fl” having lengths of  $\sim 6.4$  and  $\sim 8.8$  pc, respectively) are investigated in the I05463+2652 site. The *Herschel* temperature map depicts all these features in a temperature range of  $\sim 11$ – $13$  K. 39 clumps are identified and have masses between  $\sim 70$ – $945 M_{\odot}$ . The majority of clumps (having  $M_{\text{clump}} \gtrsim 300 M_{\odot}$ ) are distributed toward the shell-like structure. 175 young stellar objects (YSOs) are selected using the photometric  $1$ – $5 \mu\text{m}$  data and a majority of these YSOs are distributed toward the four areas of high column density ( $\gtrsim 5 \times 10^{21} \text{ cm}^{-2}$ ;  $A_V \sim 5.3$  mag) in the shell-like structure, where massive clumps and a spatial association with filament(s) are also observed. The knowledge of observed masses per unit length of elongated filaments and critical mass length reveals that they are supercritical. The filament “nw-fl” is fragmented into five clumps (having  $M_{\text{clump}} \sim 100$ – $545 M_{\odot}$ ) and contains noticeable YSOs, while the other filament “s-fl” is fragmented into two clumps (having  $M_{\text{clump}} \sim 170$ – $215 M_{\odot}$ ) without YSOs. Together, these observational results favor the role of filaments in the star formation process in I05480+2545. This study also reveals the filament “s-fl,” containing two starless clumps, at an early stage of fragmentation.

*Key words:* dust, extinction – ISM: clouds – ISM: individual objects (IRAS 05463+2652) – stars: formation – stars: pre-main sequence – stars: protostars

$^{13}\text{CO}$  1-0 観測 (Kawamura+ 1998)

- 182.0-00.3,  $V_{\text{lsr}} = -10.6$  km/s, distance = 2.1 kpc
- $dV = 1.7$  km/s,  $R_c \sim 10$  pc,  $M_{\text{cloud}} \sim 9000 M_{\text{sun}}$

データ:

Herschel

UKIRT UKIDSS GP survey

NRAO VLA Sky Survey

WISE, Glimpse360

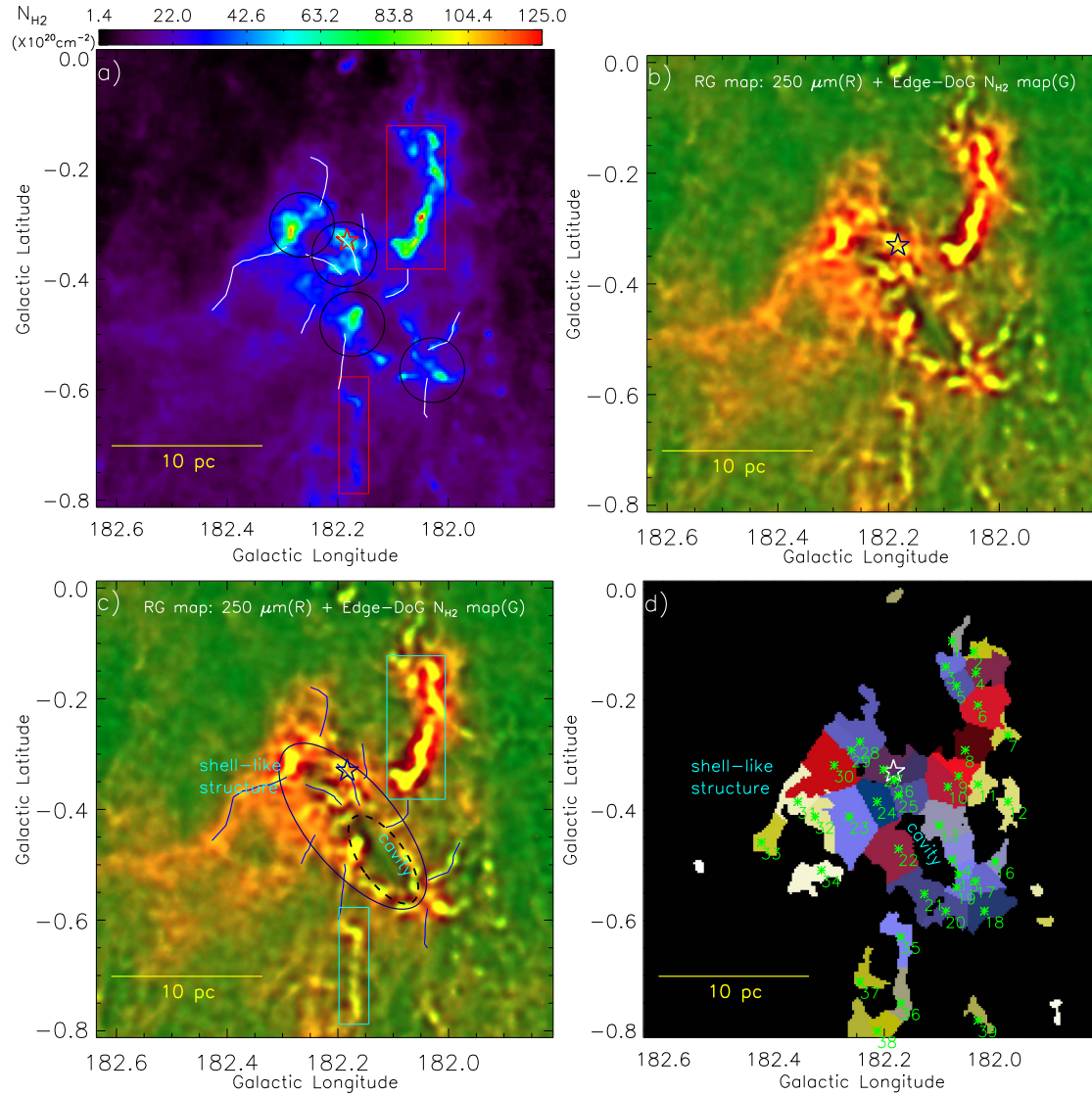


**Figure 4.** (a) *Herschel* column density ( $N(\text{H}_2)$ ) map of I05463+2652. Several filaments are highlighted by curves, which are similar to those shown in Figure 1(b). Black circles show at least four areas of high column density ( $\gtrsim 5 \times 10^{21} \text{ cm}^{-2}$  ( $A_V \sim 5.3$  mag)). The boxes also encompass two other elongated filamentary structures (“nw-fl” and “s-fl”; also see Figure 3(b)). (b) A two color-composite map (*Herschel* 250  $\mu\text{m}$  (red) and *Herschel* column density map (green) images) of I05463+2652. Here, the column density map is processed through an “Edge-DoG” algorithm. (c) It is the same as that shown in Figure 4(b). A shell-like structure and a cavity are labeled and are also highlighted by ellipses (also see Figure 2(b)). Other marked curves and boxes are similar to those shown in Figure 4(a). (d) The distribution of identified *Herschel* clumps in our probed field around I05463+2652. The identified clumps are highlighted by asterisks and the boundary of each clump is also shown in the figure along with its corresponding clump ID (see Table 1). A shell-like structure and a cavity are also labeled. In all the panels, the position of I05463+2652 is highlighted by a star. In each panel, the scale bar corresponding to 10 pc (at a distance of 2.1 kpc) is shown in the bottom left corner.

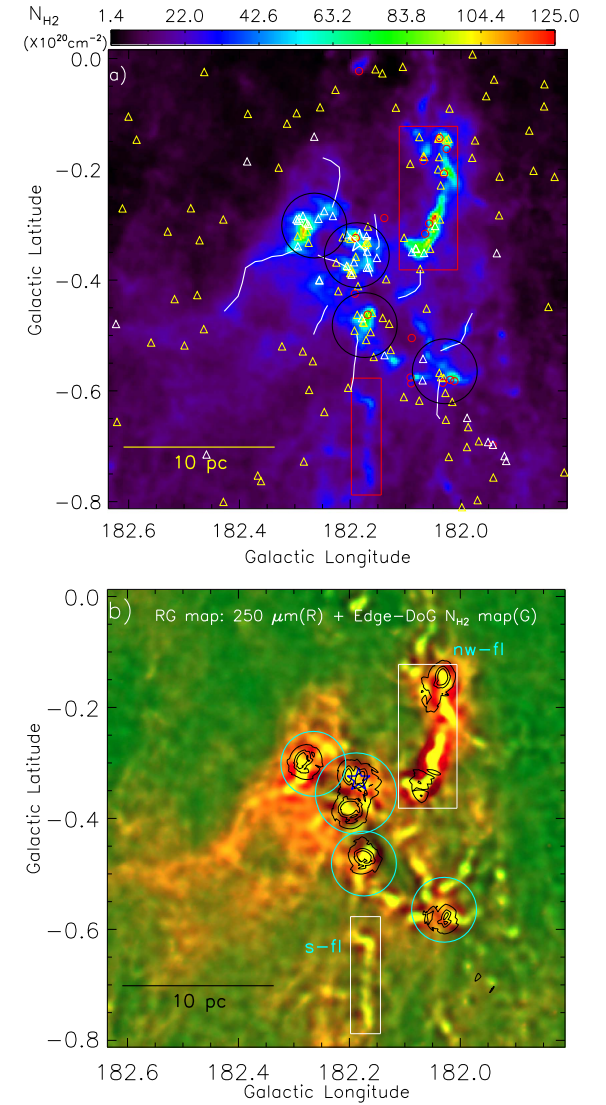


**Figure 6.** (a) *Herschel* column density map is overlaid with the identified YSOs in our selected field around I05463+2652. The marked symbols are similar to those shown in Figure 5(c). Several filaments are highlighted by curves, which are similar to those shown in Figures 1(b) and 4(a). Black circles indicate the areas of high column density ( $\gtrsim 5 \times 10^{21} \text{ cm}^{-2}$  ( $A_V \sim 5.3$  mag)). The background map is similar to the one shown in Figure 3(b). (b) A two color-composite map (*Herschel* 250  $\mu\text{m}$  (red) and *Herschel* column density map (green) images) is superimposed with the surface density contours (in black) of YSOs. The background map is similar to the one shown in Figure 4(b). The maps show the presence of clusters of YSOs toward the areas of high column density in the shell-like structure and the filament “nw-fl.” The contours are shown at  $[3, 6, 9] \times \sigma$  (where,  $1\sigma = 0.4$  YSOs  $\text{pc}^{-2}$ ), from the outer to the inner side. In both panels, the boxes encompass two elongated filamentary structures (“nw-fl” and “s-fl”; also see Figure 3(b)). In each panel, the position of I05463+2652 is highlighted by a star and the scale bar corresponding to 10 pc (at a distance of 2.1 kpc) is shown in the bottom left corner.

297  
#9

## A deep staring campaign in the $\sigma$ Orionis cluster Variability in substellar members

P. Elliott, A. Scholz, R. Jayawardhana, J. Eisloffel, and E. M. Hébrard  
arXiv:1708.03711v2

### ABSTRACT

*Context.* The young star cluster near  $\sigma$  Orionis is one of the primary environments to study the properties of young brown dwarfs down to masses comparable to those of giant planets.

*Aims.* Deep optical imaging is used to study time-domain properties of young brown dwarfs over typical rotational timescales and to search for new substellar and planetary-mass cluster members.

*Methods.* We used the Visible Multi Object Spectrograph (VIMOS) at the Very Large Telescope (VLT) to monitor a  $24' \times 16'$  field in the  $I$ -band. We stared at the same area over a total integration time of 21 hours, spanning three observing nights. Using the individual images from this run we investigated the photometric time series of nine substellar cluster members with masses from 10 to  $60 M_{\text{Jup}}$ . The deep stacked image shows cluster members down to  $\approx 5 M_{\text{Jup}}$ . We searched for new planetary-mass objects by combining our deep  $I$ -band photometry with public  $J$ -band magnitudes and by examining the nearby environment of known very low mass members for possible companions.

*Results.* We find two brown dwarfs, with significantly variable, aperiodic light curves, both with masses around  $50 M_{\text{Jup}}$ , one of which was previously unknown to be variable. The physical mechanism responsible for the observed variability is likely to be different for the two objects. The variability of the first object, a single-lined spectroscopic binary, is most likely linked to its accretion disc; the second may be caused by variable extinction by large grains. We find five new candidate members from the colour-magnitude diagram and three from a search for companions within 2000 au. We rule all eight sources out as potential members based on non-stellar shape and/or infrared colours. The  $I$ -band photometry is made available as a public dataset.

*Conclusions.* We present two variable brown dwarfs. One is consistent with ongoing accretion, the other exhibits apparent transient variability without the presence of an accretion disc. Our analysis confirms the existing census of substellar cluster members down to  $\approx 7 M_{\text{Jup}}$ . The zero result from our companion search agrees with the low occurrence rate of wide companions to brown dwarfs found in other works.

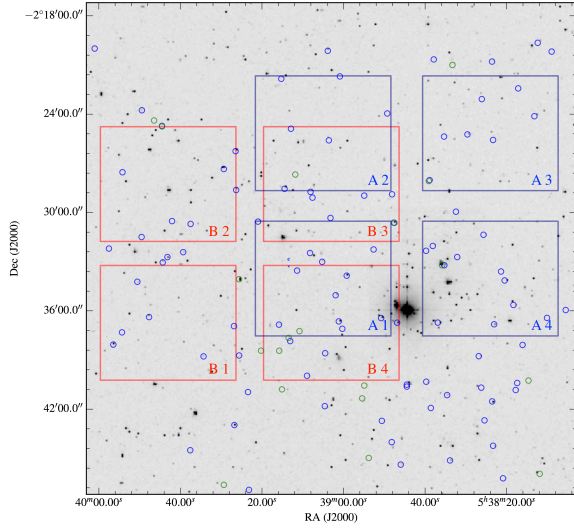


**Fig. 1.** The observed pointings of our VIMOS/VLT observations overlaid on the 2MASS  $J$ -band image. The navy blue and red rectangles are the four quadrants for Fields A and B, respectively. The blue and green sources are young and photometric candidate sources, respectively, presented in Peña Ramírez et al. (2012).

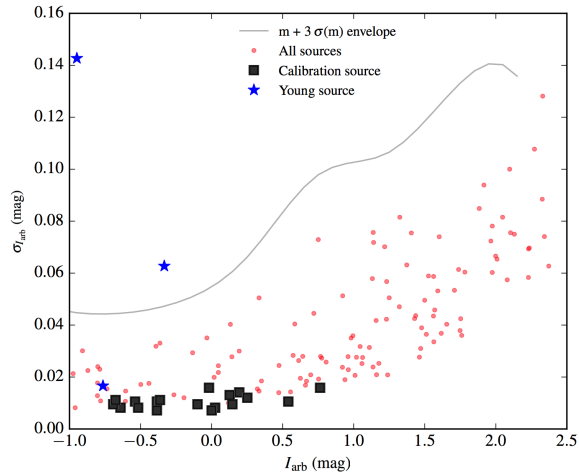


**Fig. 2.** Standard deviation of the light curves in Field A, quadrant 1 for  $\sigma$  Orionis versus median uncalibrated  $I$ -band magnitude.

**Table 1.** Basic properties of young members and photometric candidates in  $\sigma$  Orionis from Peña Ramírez et al. (2012) that are studied in this work.

Resolvable Simbad ID	RA hh:mm:ss.s	DEC dd:mm:ss	Feat. <sup>a</sup>	IR Excess	$J^b$ (mag)	$M$ ( $M_{\text{Jup}}$ )	Var? <sup>c</sup>	Comments
Variability and deep image analysis								
Mayrit 258337	05:38:38.1	-02:32:03	RV, g, d	Y(4.5, 8.0, 12.0)	15.07	56	Y	SB1, Known var.
Mayrit 396273	05:38:18.3	-02:35:39	RV, g	N	15.29	47	Y	
Mayrit 379292	05:38:21.4	-02:33:36	RV, Li, g, d	Y(12.0)	15.31	47	...	
[MJO2008] J053852.6-023215	05:38:52.6	-02:32:15	RV, g	N	16.18	29	...	
[BNM2013] 90.02 782	05:39:12.9	-02:24:54	H $\alpha$	N	16.68	24	...	
[BNM2013] 90.02 1834	05:39:00.3	-02:37:06	H $\alpha$ , d	Y(4.5, 8.0)	17.19	19	...	
[BZR99] S Ori 51	05:39:03.2	-02:30:20	g	N	17.16	19	...	
[BZR99] S Ori 50	05:39:10.8	-02:37:15	...	N	17.47	17	...	Photometric cand.
[BZR99] S Ori 58	05:39:03.6	-02:25:36	H $\alpha$ , d	Y(4.5, 8.0)	18.42	11	...	
Deep image analysis only								
[BZR99] S Ori 60	05:39:37.5	-02:30:42	H $\alpha$ , d	Y(8.0)	19.02	8	...	
[BZR99] S Ori 62	05:39:42.1	-02:30:32	H $\alpha$	N	19.14	8	...	
[BZR99] S Ori 65	05:38:26.1	-02:23:05	d	Y(4.5, 8.0)	20.30	5	...	

**Notes.** <sup>(a)</sup> RV: Radial velocity consistent with systemic cluster velocity, g: low-gravity atmosphere, Li: Lithium absorption, H $\alpha$ : Strong, broad H $\alpha$  emission, d: Presence of a disc. <sup>(b)</sup>  $J$ -band magnitude from Peña Ramírez et al. (2012). <sup>(c)</sup> Indicates if variability was identified from the analysis in this work.

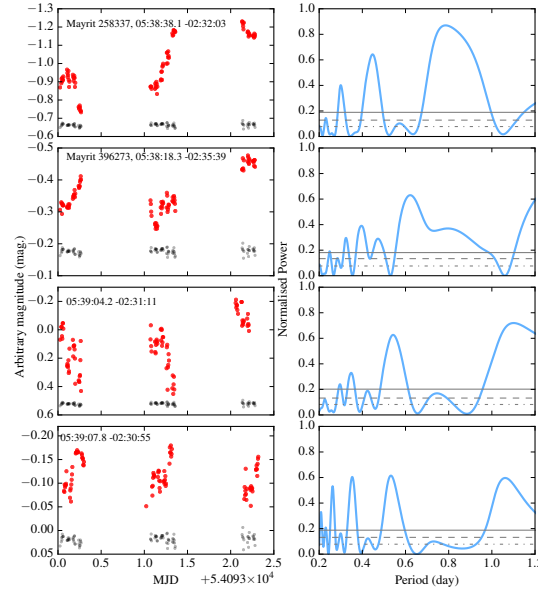


**Fig. 3.** Left panels: VIMOS light curves for the four variable sources identified in this work (Table 2). The red markers are the light curves of each source, the grey markers are the light curve of a calibration source of similar magnitude, shown for comparison. Right panels: Generalised Lomb Scargle periodograms for each variable source. The dot-dashed, dashed, and solid grey lines are  $1\sigma$ ,  $2\sigma$ , and  $3\sigma$  intervals from 1000 bootstrap samples.

- We have identified significant variability in two young brown dwarfs, one newly identified, from a sample of nine.
- Given the short time span of observations and the strong inter-night variations in their quasi-periodic signal, we could not calculate a definitive period for either object.
- The first object, Mayrit 258337 (a single-lined spectroscopic binary), shows a host of consistent properties with other young variable objects, such as correlated and variable mid-infrared magnitudes and mid-infrared excess. Therefore, its variability in the  $I$  band is most likely linked to its accretion disc.
- The second object, Mayrit 396273, has no mid-infrared excess and no significant correlation or variation in mid-infrared magnitude. The observed variability in the  $I$  band may be caused by variable extinction by large grains.
- We did not find any new low-mass potential members of  $\sigma$  Orionis using our uncalibrated  $I$ -band photometry with available UKIDSS  $J$ -band photometry, consistent with the results of Peña Ramírez et al. (2012).
- We did not identify any new low-mass companions around forty young  $\sigma$  Orionis sources in the approximate physical separation range 500–2000 au, consistent with other studies of wide multiplicity in very low-mass objects.

297  
#10

## The HIP 79977 debris disk in polarized light

N. Engler, H.M. Schmid, Ch. Thalmann, A. Boccaletti, A. Bazzon, A. Baruffolo, J.L. Beuzit, R. Claudi, A. Costille, S. Desidera, K. Dohlen, C. Dominik, M. Feldt, T. Fusco, C. Ginski, D. Gisler, J.H. Girard, R. Gratton, T. Henning, N. Hubin, M. Janson, M. Kasper, Q. Kral, M. Langlois, E. Lagadec, F. Ménard, M.R. Meyer, J. Milli, D. Mouillet, J. Olofsson, A. Pavlov, J. Pragt, P. Puget, S.P. Quanz, R. Roelfsema, B. Salasnich, R. Siebenmorgen, E. Sissa, M. Suarez, J. Szulagyi, M. Turatto, S. Udry, and F. Wildi  
arXiv:1709.00417v2

### ABSTRACT

*Context.* Debris disks are observed around 10 to 20 % of FGK main-sequence stars as infrared excess emission. They are important signposts for the presence of colliding planetesimals and therefore provide important information about the evolution of planetary systems. Direct imaging of such disks reveals their geometric structure and constrains their dust-particle properties.

*Aims.* We present observations of the known edge-on debris disk around HIP 79977 (HD 146897) taken with the ZIMPOL differential polarimeter of the SPHERE instrument. We measure the observed polarization signal and investigate the diagnostic potential of such data with model simulations.

*Methods.* SPHERE-ZIMPOL polarimetric data of the 15 Myr-old F star HIP 79977 (Upper Sco, 123 pc) were taken in the Very Broad Band (VBB) filter ( $\lambda_c = 735$  nm,  $\Delta\lambda = 290$  nm) with a spatial resolution of about 25 mas. Imaging polarimetry efficiently suppresses the residual speckle noise from the AO system and provides a differential signal with relatively small systematic measuring uncertainties. We measure the polarization flux along and perpendicular to the disk spine of the highly inclined disk for projected separations between 0.2'' (25 AU) and 1.6'' (200 AU). We perform model calculations for the polarized flux of an optically thin debris disk which are used to determine or constrain the disk parameters of HIP 79977.

*Results.* We measure a polarized flux contrast ratio for the disk of  $(F_{\text{pol}})_{\text{disk}}/F_* = (5.5 \pm 0.9) \cdot 10^{-4}$  in the VBB filter. The surface brightness of the polarized flux reaches a maximum of  $\text{SB}_{\text{max}} = 16.2$  mag arcsec $^{-2}$  at a separation of 0.2'' – 0.5'' along the disk spine with a maximum surface brightness contrast of 7.64 mag arcsec $^{-2}$ . The polarized flux has a minimum near the star < 0.2'' because no or only little polarization is produced by forward or backward scattering in the disk section lying in front of or behind the star. The width of the disk perpendicular to the spine shows a systematic increase in FWHM from 0.1'' (12 AU) to 0.3'' – 0.5'', when going from a separation of 0.2'' to > 1''. This can be explained by a radial blow-out of small grains. The data are modelled as a circular dust belt with a well defined disk inclination  $i = 85(\pm 1.5)^\circ$  and a radius between  $r_0 = 60$  and 90 AU. The radial density dependence is described by  $(r/r_0)^\alpha$  with a steep (positive) power law index  $\alpha = 5$  inside  $r_0$  and a more shallow (negative) index  $\alpha = -2.5$  outside  $r_0$ . The scattering asymmetry factor lies between  $g = 0.2$  and 0.6 (forward scattering) adopting a scattering-angle dependence for the fractional polarization such as that for Rayleigh scattering.

*Conclusions.* Polarimetric imaging with SPHERE-ZIMPOL of the edge-on debris disk around HIP 79977 provides accurate profiles for the polarized flux. Our data are qualitatively very similar to the case of AU Mic and they confirm that edge-on debris disks have a polarization minimum at a position near the star and a maximum near the projected separation of the main debris belt. The comparison of the polarized flux contrast ratio  $(F_{\text{pol}})_{\text{disk}}/F_*$  with the fractional infrared excess provides strong constraints on the scattering albedo of the dust.

**Key words.** Planetary systems – Scattering – Stars: individual object: HIP 79977, HD 146897 – Techniques: high angular resolution, polarimetric

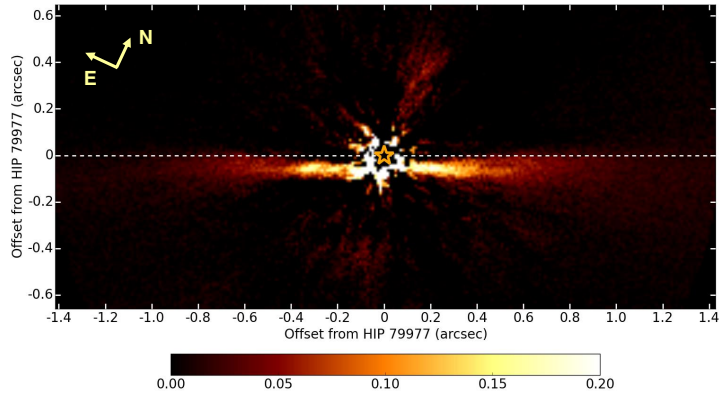


**Fig. 2.** Composite image of debris disk around HIP 79977 with the VBB and I-band filters obtained with LOCI data reduction. The original data were  $3 \times 3$  binned to reduce the effect of the noise. The position of the star is marked by an asterisk in orange. The white dotted line shows the position of the expected lines of nodes for an inclined disk ring. The color-scale is given in arbitrary units.

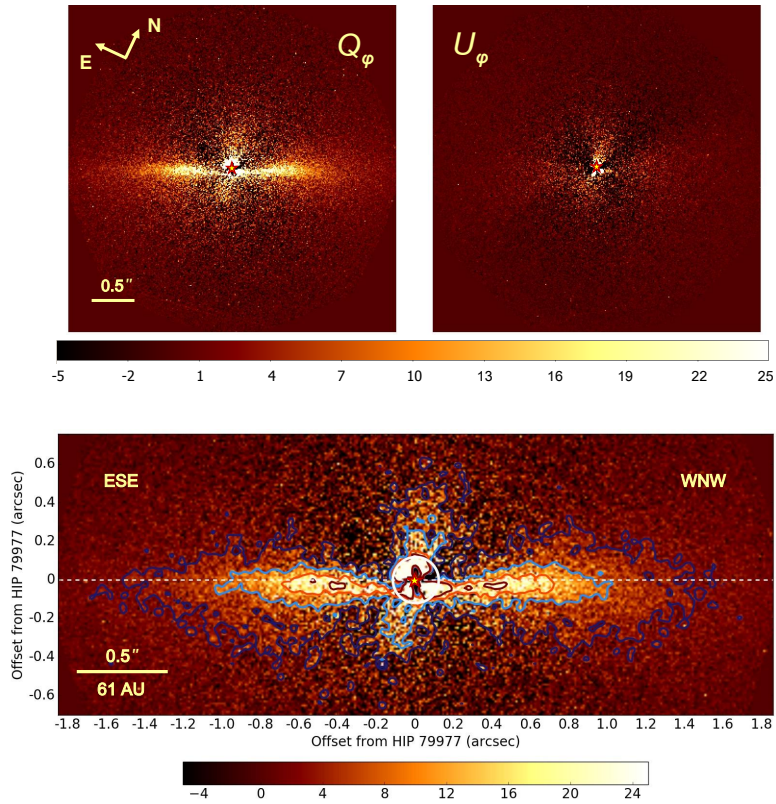


**Fig. 4.** Polarimetric differential imaging data of HIP 79977 with the VBB filter (590-880 nm). The original data were  $3 \times 3$  binned to reduce the noise. The position of the star is marked by an asterisk in red. The upper panel shows  $Q_\phi$  (left) and  $U_\phi$  (right) images. Lower panel: Isophotal contours of polarized light overlying  $Q_\phi$  image. The contours were measured from the  $Q_\phi$  image smoothed via a Gaussian kernel with  $\sigma = 1.5$  px. Contour levels are given for 3 (blue line), 9 (light blue), 15 (orange) and 21 (red) counts per frame per binned pixel. The white dotted line shows the position of the expected ring axis. The region inside the white stellarcentric circle with radius  $\sim 0.12''$  is dominated by strong speckles variations. The color-bars show the counts per binned pixel.

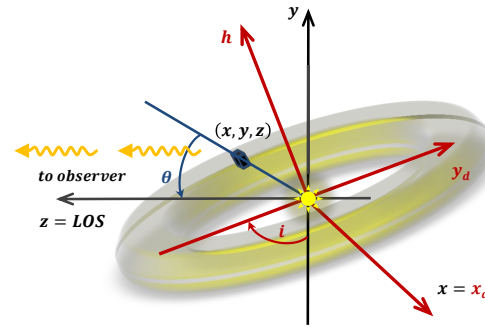


**Fig. 7.** Illustrative sketch of the debris disk with inclination  $i$  and coordinate systems  $(x, y, z)$  and  $(x_d, y_d, h)$  used in model. The small blue cube at scattering angle  $\theta$  marks the position  $(x, y, z)$  of a grid element with grain number density  $n(x, y, z)$ .

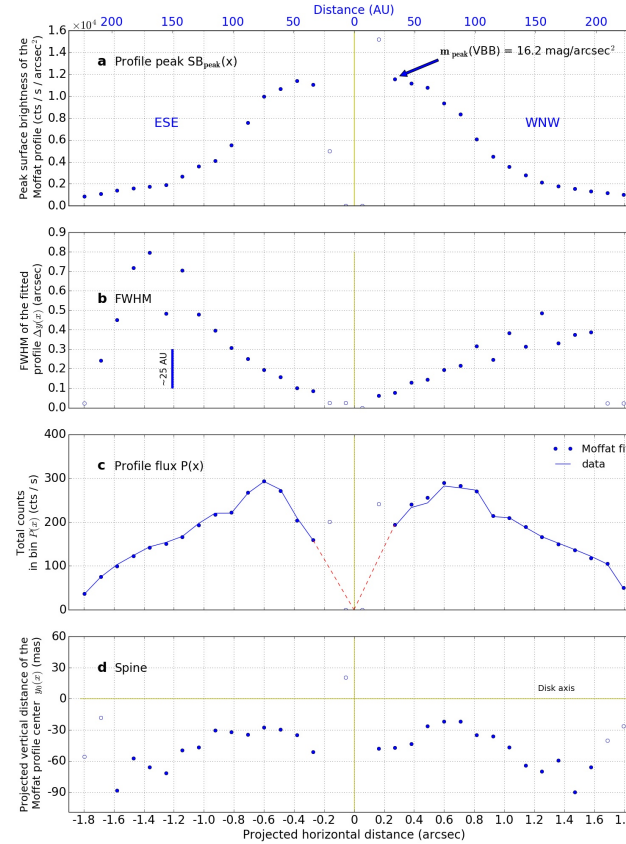


**Fig. 6.** HIP 79977 debris disk properties along the axis  $x$ . The individual points give parameters of the Moffat profile of the vertical cross section as shown in Fig. 5 and described in Sect. 4.2. From the top to the bottom: (a) the profile peak  $SB_{\text{peak}}(x)$ , (b) FWHM, (c) vertically integrated flux  $P(x)$ , and (d) spine distance from the disk major axis  $y_0$ . The vertically integrated profile flux  $P(x)$  is calculated as a mean surface brightness in a  $0.1'' \times 1.8''$  bin. At separations smaller than  $x \approx 0.2''$  the systematic uncertainties are increased and open circles mark the low S/N points. The vertical yellow line indicates the position of the star.

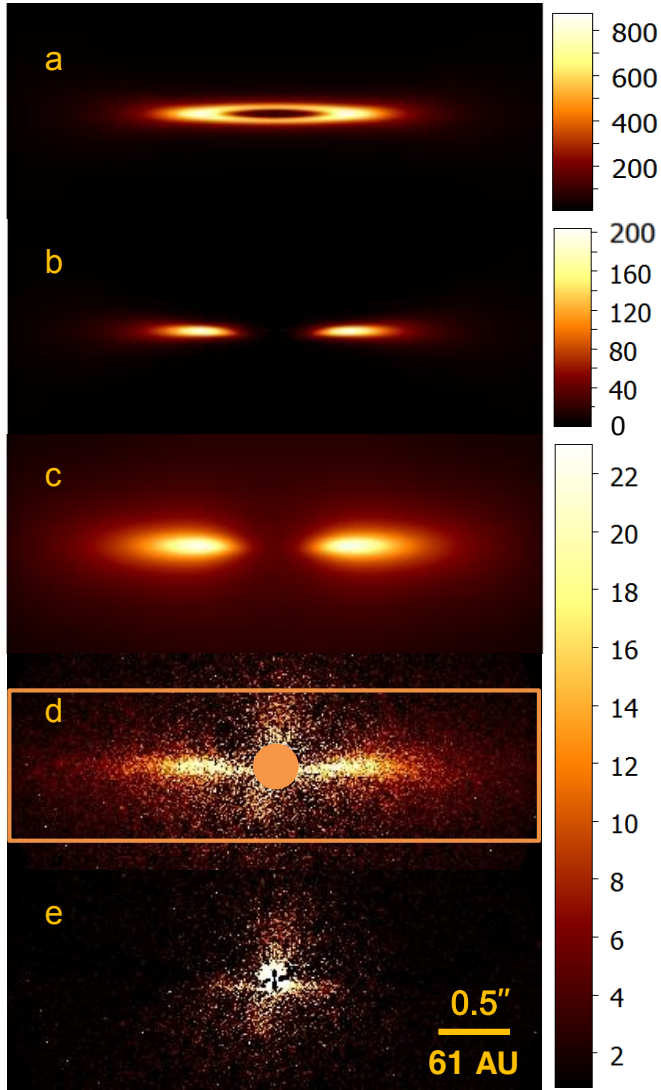


**Fig. 9.** Comparison of the best-fit model with the  $Q_\varphi$  image. (a) Image visualizing the dust distribution in the disk. (b) Model image of the polarized light non-convolved with PSF. (c) Model image of the polarized light convolved with the instrumental PSF. (d)  $Q_\varphi$  image from the data. The rectangular area outlined with an orange box shows the minimization window as described in the body text. The orange circle marks the central region of the image excluded from the  $\chi^2$  evaluation. (e) Residual image obtained after subtraction of the PSF-convolved model image (c) from the  $Q_\varphi$  image (d). Color-scales of images (a) and (b) are given in arbitrary units. The color-bar for images (c), (d) and (e) shows polarized flux in counts per binned pixel.

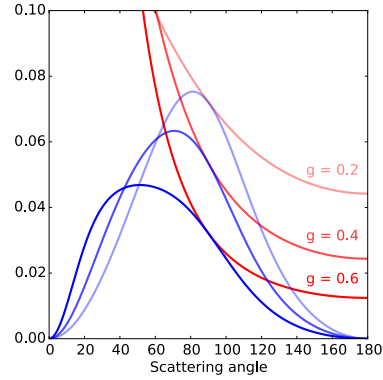


**Fig. 8.** Scattering phase function for the polarized light (blue) for three different asymmetry parameters  $g_{sca} = 0.2$ ,  $g_{sca} = 0.4$ , and  $g_{sca} = 0.6$ . Red lines show the corresponding Heyney-Greenstein functions for  $f(\theta, g_{sca})$ .

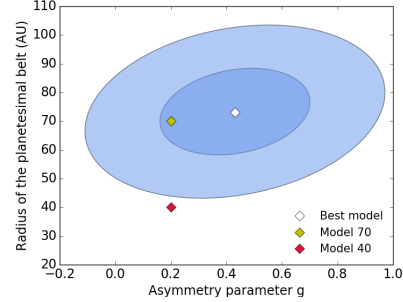


**Fig. 12.** Two-dimensional constraints on the radius of the planetesimal belt  $r_0$  and the asymmetry parameter  $g_{sca}$  for HIP 79977. The contours show the 68% and 95% CL regions for the model sample and the dots point out the locations of the described models in this parameter plain.

**Table 3.** Grid of parameters for the  $5.28 \cdot 10^6$  models and resulting parameters for the best fit model. Also given are the parameters of two selected comparison models ("Model 70" and "Model 40").

Parameter	Range	Step of linear sampling	Best model		Model 70	Model 40
			mean value	68% CL		
Radius of belt $r_0$ (AU)	[30, 90]	10	73	16	70	40*
Inner radial index $\alpha_{in}$	[1, 10]	1	5.0	2.8	2.0*	2.0*
Outer radial index $\alpha_{out}$	[-6, -1]	0.5	-2.5	1.4	-3.0	-2.5
Scale height $H_0$ (AU)	[0.5, 3.5]	0.5	2.3	0.7	1.5	0.5*
Vertical profile $\gamma$	[0.5, 2.5]	0.5	0.9	0.6	1.0	1.0
Flare index $\beta$	[0.5, 4.5]	1	2.2	1.4	2.5	3.5
Inclination $i$ ( $^\circ$ )	[82, 87]	1	84.6	1.7	85.0	82.0*
HG parameter $g_{sca}$	[0.0, 0.9]	0.1	0.43	0.25	0.20	0.20
Scaling factor $A_p$	-	-	9.04	-	4.03	3.10

Notes: \* Parameter value lies outside the 68% confidence interval.

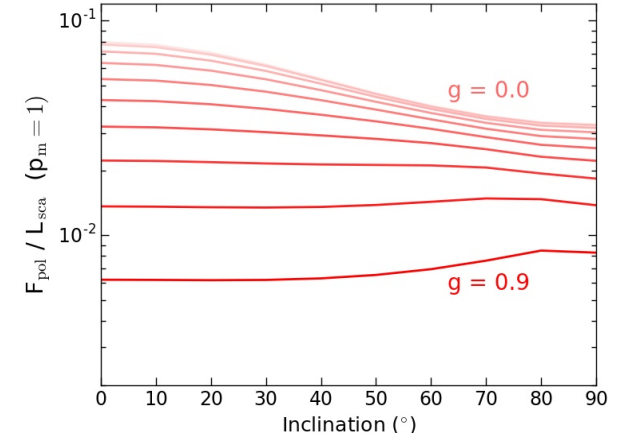


**Fig. 13.** Ratio of polarized flux to the scattered light luminosity for optically thin debris disks as a function of disk inclination and scattering asymmetry parameter  $g_{sca}$  (plotted for  $g_{sca} = 0.0, 0.2, 0.3, \dots, 0.9$ ). The ratio is independent of the disk geometry and follows from the scattering phase functions as shown in Fig. 8.